Performance of PIV and PTV for granular flow measurements

Devis Gollin[1] · Wernher Brevis[1] · Elisabeth T. Bowman[1] · Paul
Shepley[1]

Abstract As tools and techniques to measure experimental granular flows become increasingly sophisticated, there is a need to rigorously assess the validity of the approaches used. This paper critically assesses the performance of Particle Image Velocimetry (PIV) and Particle Tracking Velocimetry (PTV) for the measurement of granular flow properties. After a brief review of the PIV and PTV techniques, we describe the most common sources of error arising from the applications of these two methods. For PTV, a series of controlled experiments of a circular motion is used to illustrate the errors associated with the particle centroid uncertainties and the linear approximation of particle trajectories. The influence of these errors is then examined in experiments on dry monodisperse granular flows down an inclined chute geometry. The results are compared to those from PIV analysis in which errors are influenced by the size of the interrogation region. While velocity profiles estimated by the two techniques show strong agreement, second order statistics, e.g. the granular temperature, display very different profiles. We show how the choice of the sampling interval, or frame rate, affects both the magnitude of granular temperature and the profile shape determined in the case of PTV. In addition, the determined magnitudes of granular temperature from PIV tends to be considerably lower when directly measured or largely overestimated when theoretically scaled than those of PTV for the same tests, though the shape of the profiles is less sensitive to frame rate. We finally present solid concentra-
tion profiles obtained at the sidewalls and and examine their relationship to the determined shear rate and granular temperature profiles.

Keywords Particle Image Velocimetry (PIV) · Particle Tracking Velocimetry (PTV) · Sources of error · Granular flows

Devis Gollin
devis.gollin@sheffield.ac.uk

[1] Department of Civil and Structural Engineering, University of Sheffield, Western Bank, Sheffield, S10 2TN, UK

1 Introduction

The study of granular flows has become increasingly popular in recent years. Such flows encompass both granular chute flows for industrial applications and also landslide and debris flows in the geophysical context. In laboratory experiments, non-invasive measurements of motion are usually obtained using imaging techniques such as Particle Image Velocimetry (PIV) and Particle Tracking Velocimetry (PTV). These techniques are broadly used to estimate the velocity of groups of particles or movement of single particles.

A number of investigations of granular flows in which imaging techniques are used have been reported in the literature. PIV applications include the works of [22, 48, 28, 38, 43, 25, 5, 14]. Studies that use PTV include the works of [50, 7, 26, 6, 11, 31]. PIV allows estimation of the velocity by performing cross-correlation within interrogation regions of small tracer particles or particle texture. Improvement of this technique has been widely reported in the literature (e.g. [3]) in the fields of fluid mechanics ([1]) and geomechanics (e.g. [53, 46]).

Another method of analysis developed for the case of low seeding densities is PTV. This relies on the ability to track individual particles, an attractive characteristic for the study of granular flows. In the last decades, efforts made to improve PTV together with relatively recent algorithms have proved its reliability also at high

densities. Therefore, PTV has become the main method of choice to collect measurements from moving particle flows.

Recent research has focused on describing granular flows according to their microscopic behaviour, e.g., when investigating the transfer of momentum caused by the particle interactions via collisions. This concept was first presented by [8] and later introduced in the kinetic theory of granular gases ([36]). Since extension of this theory to dense granular flows (e.g. [27]) there has been the need to obtain measurements at particle level. Information obtained at this level may be used to improve and support fundamental works devoted to the validation and refinement of both existing and new theoretical models. However, without due caution the applications of these techniques can result in misleading interpretation of the physical quantities in question.

In this paper we do not describe in detail the variety of PIV and PTV algorithms that can be found in the literature, rather we focus our attention on simple but important experimental parameters. Indeed, we show here that the reliability of results is directly related to such parameters as the temporal resolution (camera frame rate) and the spatial resolution (pixel density) of the measurements.

The primary motivation for this work is to begin to develop basic guidelines which may be adopted when PIV and PTV are employed to investigate granular flows. We first give a general introduction of PIV followed by a more exhaustive description of PTV. Then we present the most relevant sources of error arising from the application of these two techniques. Here the methods we have devised to compensate for PTV errors are also explained. Finally, we examine the performance of these two approaches to the descriptions of dry granular flows down an inclined chute geometry.

2 Review of PIV and PTV methods

While three-dimensional PIV and PTV have been proposed ([33,42]), here we focus only on their two-dimensional implementations, i.e., the computed displacement is obtained in only two directions (e.g. streamwise and transverse flow directions).

PIV and PTV are image velocimetry techniques that were originally developed in the field of experimental fluid mechanics for the study of single- and multi-phase fluid flows. In this context the methodological principle is to add tracer particles to the flow, i.e. assuming that they move under the action of the flow structure of interest. While a fluid requires seeding with particles to create features upon which image processing can

operate, granular flows have their own texture in the form of natural or idealized particles (usually spheres) which can be individually tracked. With an appropriate number of tracers or particles, a rigorous reconstruction of the entire flow and its essential properties can be achieved. The flow field is usually illuminated by a source of light (lighting system or laser light) to highlight the particle locations. A CCD or CMOS based camera is then used to capture a sequence of images separated by a defined time interval. The displacement of a characteristic interrogation region for PIV or a singular particle for PTV is determined differently according to the technique used.

PIV is a well-established technique and exhaustive reviews may be found in the literature, for example, in [4]. PIV invokes statistical methods to track the displacement of a small group of particles. The common approach is to divide the entire field-of-view into smaller regions, called interrogation areas (or patches ([53]). Extracting the displacement information between two consecutive images is performed by cross-correlating the interrogation areas at two sequential time steps using the calculation of correlation via Fourier Transform. Eulerian velocity vectors of the assemble of particles in the sub-images are provided in a regular raster by dividing each displacement by the time step chosen for the acquisition.

An alternative image processing technique that is suitable to obtain the velocity field is two-frame particle tracking via PTV. Generally, a particle image has a brightness pattern with a peak near its centroid, with brightness progressively decreasing one pixel away from this peak. The process followed by PTV begins with the individualization of particles and the estimation of their centroids. Perhaps the simplest method for individual-particle detection from the image intensity distribution is the single-threshold binarization of a binarized image, commonly referred to as image segmentation ([4]). Once found the particle is labelled, its position is calculated by means of a centre-of-mass estimator. This method finds its best applications in low density flows where the edge of each particle can be clearly identified. However, in dense granular flows, particles move randomly creating a non-homogeneous distribution of the intensity matrix over time. Moreover, due to the high concentration, particles are prone to overlap, appearing with no sharp edges, leading to spurious detection or loss of the particle data. In order to handle such cases and also situations where the particle images are partly varied with respect to their size, mean brightness level, and intensity-distribution profile, other methods are available, such as dynamic threshold binarization ([34]) and particle-mask-correlation ([47]). In dynamic
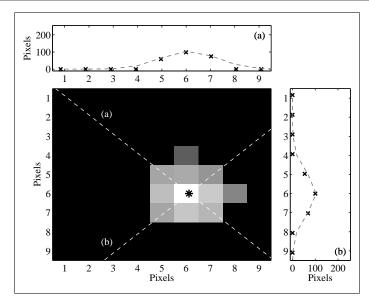
Fig. 1 Determination of the particle centroid. To find the the peak of the distributions, i.e. the centre coordinates, the algorithm selected values (x-marks) of the intensity matrix are fitted by two curves (dashed-lines) in x- and y-direction, (a) and (b), respectively.

threshold binarization, the binarization threshold is adjusted according to the mean intensity of each particle. This is done in such a way that the contrast or difference with the image background is kept constant. For the method to be successful the base threshold needs to be always higher than the noise level. In the particle-mask-correlation method, a Gaussian reference mask (i.e. a matrix) is convoluted to the intensity distribution around each particle. The centroid of the particle is identified when the correlation value between the mask and a sub-matrix, of the same size of the mask and centred on each image pixel, is above a predefined threshold level. Both methods, dynamic threshold binarization and the particle-mask-correlation method, are able to detect overlapped particles and can estimate their centroid position with sub-pixel accuracy. However, their limitation lies in the fact that they assume that the shape and intensity distribution is that of a circular particle.

In case of dynamic threshold binarization, the sub-pixel accuracy is achieved by using techniques similar to the one used for the binary method (i.e. centre-of-mass estimator). In the particle-mask-correlation method, the threshold correlation level is chosen once, before the analysis, and is taken to be representative of all image particles. However, this can lead to uncertainties in the particle centroid estimation due to differences in intensity matrix of nearly overlapping particles and those at the margins. An accurate estimation of the centroid position can be obtained by fitting a presumed functional shape to the intensity matrix centred individually on each particle. Generally, the estimate of a given param-

eter (e.g. the sub-pixel particle position) is attained by minimizing the sum of the squared difference χ^2 between the observation $\tau[m,n]$ in a MxN-pixel domain and a suitable model $h(X, Y; \boldsymbol{\theta})$ with respect to a parameter vector $\boldsymbol{\theta}$:

$$\chi^2 = \sum_m^M \sum_n^N \left(\frac{\tau[m,n] - h(X_m, Y_n; \boldsymbol{\theta})}{\sigma_{m,n}} \right)^2 \qquad (1)$$

where $\sigma_{m,n}$ is a weighting factor and $\tau[m,n]$ the pixel intensities in the interrogation region. For circular particles the functional shape is well approximated by a Gaussian distribution and the parameter vector would consist of $\boldsymbol{\theta} = (\tau_{00}, X_0, Y_0, d)$, that is, the amplitude (τ_{00}), a guessed particle location (X_0, Y_0) and the characteristic diameter (d). The guessed particle location can be acquired, for instance, by the use of one of the other methods mentioned above. It may be expected that the least-square fit in Eq. 1 will give very accurate results in the case of low density flows. Conversely, in highly concentrated flows the size and the shape of the particle image are determined by the aforementioned factors (e.g. random movement and particle overlap). Care should be taken if the parameter estimates are not near the minimum of χ^2 or when a large number of fitting parameters are used. Otherwise the result may be an excessive increase in computational time which is a major drawback of this method.

A characteristic application of this method is illustrated in Fig. 1. A guessed location is first generated using the particle-mask-correlation method by correlating

the Gaussian reference matrix to the particle image. A portion of the original image containing the particle of interest is then extracted around this value (surrounding particles are masked out). This information is then used as part of the parameter vector in Eq. 1. This equation enables the refinement of the guessed particle location, yielding a higher precision estimate. During the processing of the data, curves based on the presumed functional shape are fitted to the intensity sub-matrix (each curve gives the centroid coordinate in respect of one axis). The process stops when the sum of squared residuals (i.e. the difference between an observed value and the fitted value provided by the model) is minimized.

Once the particle positions are found and stored, the next step is to track a large number of particles over time in order to achieve high spatial resolution (in the limiting case of steady flows) and obtain accurate results. Low seeding densities has generally been deemed the limiting case for PTV and the challenge of the tracking algorithms for use in measuring granular flows has been to achieve applicability to much higher particle densities. To do this, different tracking algorithms have been proposed, for example, [17] proposed a hybrid technique that uses PIV results to guide the particle matching algorithm and more recently [13] presented a two-stage integrated approach that combines cross-correlation with a relaxation algorithm. In the latter, during the cross-correlation phase the interrogation windows are centred on each particle candidate in the first image and a particle match is found in the second image when the highest correlation coefficient is detected. However, particle patterns associated with the interrogation areas can suffer from strong deformation due to non-linear gradients in the field. The consequence is a drop in the correlation level which would decrease the reliability of the PTV analysis. To improve the performance, the relaxation method is then applied to those unmatched candidates that were disregarded during the cross-correlation phase. Hence this method is based on the probability of particle matching between two frames defined for every possible pair of particles. This approach enables the particle-matching probability to be updated using the probabilities of the neighbouring particles which are then iterated until all the probabilities remain almost constant ([34]). This strategy was found to be effective in establishing the correct inter-particle links from the others, as was shown by a higher value of the yield parameter Y_i ([24]) compared to similar approaches. The yield Y_i is obtained from synthetic benchmark studies and it is defined as the ratio between the known number of particle displacements available between two images and the valid displacements recovered from the images. Ultimately, the merits of this specific algorithm are its applicability to complex flows with local shearing boundaries and relatively strong velocity gradients. For a complete review the reader may refer to [13].

So far we referred exclusively to two-frame methods where measurements are taken between recordings separated by two different acquisition times. The operational principle of these methods differs from multi-frame approaches where information over more than two successive frames is required. Multi-frame PIV has been proposed ([21]) primarily with the scope of increasing the dynamic velocity range (the ratio of the maximum velocity to the minimum resolvable velocity ([2]) in PIV. However this technique requires limited out-of-plane loss-of-correlation and good quality images to produce enhanced measurement accuracy. Multi-frame methods can also be applied to PTV ([16]) to reduce the relative error on the measured displacement and to enhance the robustness of the image particle pairing. Similarly to PIV they suffer from the loss of particle image pairs at the image margins. This inconvenience can be overcome, however, in the case of volumetric measurements therefore making it particularly suitable for three-dimensional PTV ([16]). Multi-frame methods are an attractive alternative that can be used to improve the performance of the algorithms, however measurement uncertainties are still associated with the centroid estimation and the choice of the optimal temporal separation of the recordings.

3 Unit description

In the following the analyses refer to particles of the same size with a characteristic mean diameter d'=1.5 mm and using the gravitational acceleration $g' = 9.81$ ms^{-2}. Our results are given in nondimensional form by defining the following normalization for the distances, times, velocities, granular temperatures (a measure of the velocity fluctuations) and shear rates: $d = 1$, $t = t'/\sqrt{d'/g'}$, $\boldsymbol{V}_{(u,v)} = \boldsymbol{V}'_{(u,v)}/\sqrt{g'd'}$, $T = T'/g'd'$ and $\gamma = \gamma' \cdot \sqrt{d'/g'}$, where $t', \boldsymbol{V}', T'$ and γ' indicate the respective dimensional forms.

4 Experimental investigation of sources of error

Without due caution, PIV and PTV can generate errors that severely affect the results. While the complete removal of these is practically impossible, some useful guidelines can be followed to minimize them. Here we briefly summarize some notions of PIV analysis useful
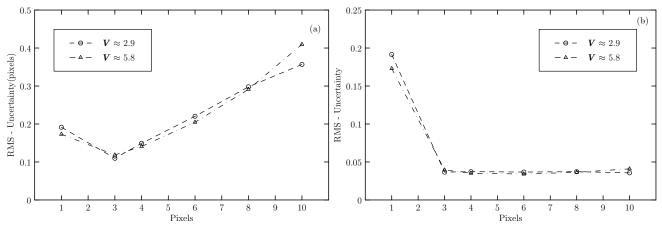
Fig. 2 Particle position uncertainties associated with a single particle undergoing a circular motion. Data are shown for two different rotational velocities: ≈ 2.9 (o) and ≈ 5.8 ($\triangle$). (a) Uncertainty versus particle diameter; (b) ratio of uncertainty to respective particle diameter. For particle tracking the minimum error is found when the particle image is 3 pixels in diameter.

to obtain valid results while more in-depth experimental investigations are described for PTV.

4.1 PIV error type and reduction

Although PIV has been mainly implemented for fluids and for pseudo-static geotechnical problems, we report here a common framework which we hope may also help the analysis of granular flows. The choice of the interrogation window size (or patch) has a strong influence on the PIV results ([23]). This parameter would depend on the experimental conditions (i.e lighting, texture, etc.) and the particle diameter. In the simple case of monodisperse flows, to increase the level of accuracy it is necessary to increase the image density N_i, i.e., the mean number of particles per interrogation window. The signal strength (the peak of the correlation matrix) increases when the number of particle images in the interrogation domain increases. Also the noise (i.e. the random correlations) is expected to increase in proportion to the image density. However, when the correlation is normalized with respect to the highest peak, the relative noise level (defined as the highest random correlation peak) decreases with increasing N_i. Examination of the normalized correlation function has shown that for a correct peak detection, the mean number of particles per interrogation area should vary between 5 and 10 ([4]). Additionally, empirical estimates for the optimal particle image diameter suggest a range that varies from 2 to 4 pixel units ([37,17]). Note that this is maybe true for spherical particles, although other particle shapes are also possible.

The boundaries of a granular flow can be frictional and generate local shearing. For instance, granular flows down chute geometries with highly frictional bottom boundaries form shearing layers, producing an in-plane velocity gradient. For methods that use standard static spatial domain correlation (i.e. when the shape of the interrogation region is fixed) in the vicinity of the bottom boundary, faster particles may leave the sub-images and the remaining slower particles act to generate in-plane loss-of-correlation, hence biasing the displacement estimates. Following [29] we will refer to this as gradient biasing. To reduce this error, the experimenter may resort to algorithms that allow iterative sub-image deformation ([40,41]). This type of scheme starts with a standard static correlation pass over the entire image. This pass then provides an initial estimated displacement vector for each node (nodes are found in the corners and the centre of the sub-image). The results are then used to determine the amount by which to dynamically deform the second sub-image. In highly sheared flows the interrogation accuracy and robustness is significantly improved. However, the computational cost is generally increased owing to the iterative structure of such advanced algorithms, and by the additional image re-sampling process ([41]).

4.2 PTV error type and reduction

PTV does not suffer from gradient biasing since particles are tracked individually and the particle image is not affected by displacement gradients. However, PTV operations inherit two main sources of error, namely the inaccuracy in determining a particle position and errors arising from the linear approximation of the particle trajectory during the time taken to move from one image to the next. Here we describe the errors and simple investigations designed to determine their magnitude in more detail.
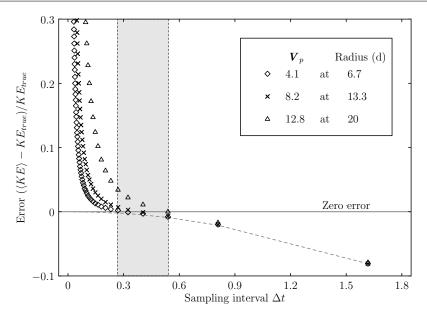
Fig. 3 Velocity errors associated with particles undergoing a circular motion at different velocities ($\mathbf{V_p}$) and radii. The value of $\langle KE \rangle$ is compared with the true kinetic energy $KE_{true} = m|\mathbf{V}_p|^2/2$ for different sampling intervals (Δt). Positive errors due to particle position uncertainties arise at small Δt (i.e. fast frame rate) whereas negative errors originate as a result of particle acceleration at large Δt (i.e. slow frame rate). The dashed-line in the negative region represents errors produced by particle acceleration only. There is a range (shaded area) along the zero-error line where the total error should be the smallest.

4.3 Particle position error

Particle position error can induce unrealistic disturbances to the measured velocity field. It is likely to be significant at very high acquisition rates due to the large relative errors induced by the centroid estimates in the total displacement. In Sec. 2 it was pointed out that there are different algorithms to detect particles and determine their locations. [17] suggested that the optimal algorithm may also be a function of particle image diameter (i.e. the diameter of the particle in number of pixels). Based on this consideration, we experimentally investigated the effect of particle size on centroid-detection error during a rotational motion. The motivation for using a circular motion was to facilitate the experimental procedures hence allowing changes in lighting conditions and camera settings while isolating the motion of an individual particle and providing the possibility of changing its position (or radius) with respect to the centre of the circular motion.

An aluminium disk covered with matt black paint was mounted on an electric motor to allow for rotation. A single white spherical particle taken from our experimental monodisperse flows (see Sec. 4) was then glued onto the disk contrasting with the dark background. Knowing the radius of the particle from the midpoint of the disk allowed a comparison to be made of the measurements with the true particle positions during circular motion. Measurements were taken for different

particle image diameters by outdistancing the camera. We varied the rotation speed and the acquisition frequency and found that they had negligible effect on the centroid-detection error magnitude. In addition, the results from the particle-mask-correlation method alone and its implementation with a least-square fit collapsed onto the same curves.

Fig. 2 (a,b) presents data for two rotational speeds. Note that in Fig. 2 (a) a minimum error is found for a particle image diameter of 3 pixels. That is, when the particle is approximated by an intensity profile which spans 3 pixels in diameter and with an intensity peak located in its centre, the sub-pixel position estimated using the three-point Gaussian approach performs best. For smaller diameters, measurements are primarily influenced by pixel-locking, whereas for larger diameters, the Gaussian fit tends to be skewed, acting to bias the particle positions. At 3 pixels we expected the magnitude of the RMS error to be close to zero, however, added to the uncertainties of the particle-mask-correlation method is a slight eccentricity of the disk that affected all of our measurements. A further control depicted in Fig. 2 (b) was made by dividing the uncertainty by the respective particle diameter. This plot shows that 3 pixels is again the minimum size of particle that should be considered. The ratio being somewhat flat for diameters larger than 3 pixels suggests that the result is insensitive to the choice of particle image larger than this value.

4.4 Linear approximation error

The second source of error is associated with the acceleration of the particles, i.e. that the real particle trajectory is approximated by linear displacement. This error is strongly affected by the choice of the acquisition frequency (or frame rate). [19] pointed out that a high frame rate is not always necessary to capture the true behaviour of the process under analysis. The simplest tracking method assumes that the particle travels between two images in a straight line at a constant speed. If the positions of a particle before and after a time interval Δt are $\mathbf{r}_i$ and $\mathbf{r}_{i+1}$ respectively, where $\mathbf{r}_i = (x_i, y_i)$, then the velocity $\boldsymbol{V}_i(u_i, v_i)$ can be estimated as:

$$\boldsymbol{V}_i = \frac{\mathbf{r}_{i+1} - \mathbf{r}_i}{\Delta t} \qquad (2)$$

In the work of [19] a uniform circular motion was used to show the error arising from the particle accelerations. Assuming zero position error, at large Δt the two-frame tracking method in Eq. 2 approximates this ideal circular motion to that of a polygon. At smaller Δt, the polygon has more sides, resembling the circle more closely.

When the particle position uncertainties are added to the process, the polygon deforms in a manner proportional to the magnitude of the error. Motivated by this and having information about the particle position errors from our previous analysis, we reproduced an experiment similar to that of [19]. A simple simulation was carried out where a single particle performs a uniform circular motion. A position error with maximum magnitude equivalent to that at 3 pixels, as in Fig 2, was randomly added to the particle. The distorted positions of the particle were updated during motion and recorded at different sampling intervals Δt. The velocity calculated in Eq. 2 was then used to compute a time series for the kinetic energy, $KE(t) = m|\mathbf{V}(t)|^2/2$, and the ensemble average, $\langle KE \rangle$, was extracted over 1000 circular periods. The values of $\langle KE \rangle$ were then compared to the true kinetic energy $KE_{true} = m|\mathbf{V}_p|^2/2$, where $\mathbf{V}_p$ is the selected particle velocity having zero position error (i.e. the radius is constant).

We varied the radius of the particle from the centre in order to change the magnitude of $\mathbf{V}_p$ under the same experimental condition. The influence of the sampling interval Δt was also analysed. The choice of differing radius, and as a consequence $\mathbf{V}_p$, is based on the fact that in a typical free-surface granular flow the velocity profile changes with depth, i.e. a typical measurement is exposed to a large dynamic range. We chose three different velocities $\mathbf{V}_p$, and radii representative of our

experiments: 4.1 at $6.7d$, 8.2 at $13.3d$, and 12.8 at $20d$, respectively. The data produced from these simulations are reported in Fig. 3.

Fig. 3 is useful to illustrate the combination of errors. Positive errors that increase the measured KE above the true value, above the zero-error line, originate due to the enhanced influence of centroid detection errors relative to the total displacement between two time intervals. This issue becomes increasingly severe for small sampling intervals (i.e. fast frame rate). Conversely, negative errors that decrease the measured KE are mainly due to the error involved in approximating the particle displacements to a straight line (Eq. 2). It is evident that for large sampling intervals, the real particle trajectories developed during their normal evolution is non-linear (e.g. curved). This means that the movement is under sampled and as a consequence it can result in a strong aliasing of the measured position signal. For reference, the dashed-line in Fig. 3 represents the error due to this effect only. This source of error is effective for large Δt (i.e. for slow frame rate). However, there is a value of Δt when the data crosses the zero-error line, that corresponds to the minimization of errors. Such information can be used to help the choice of a sampling interval that reduces the total error within the range of velocities considered for a given experiment.

The velocities $\mathbf{V}_p$ analysed here with their respective radii yield a sampling interval that ranges approximately between 0.26 and 0.54 (shaded area in Fig. 3), corresponding roughly to 150 fps (frames per second) to 350 fps. Within these values the expected total error should be minimized. Notably, Fig. 3 suggests that there is no unique value of Δt suitable for examining the whole of a granular flow. Best practice would then require a combination of different acquisition frequencies obtained by analysing different ROI at different Δt. However, we also need to consider that in most physical experiments, particles do not experience the same idealized circular motion as investigated here, with the motion of individual particles varying from that of surrounding ones. Hence, while the values reported in Fig. 3 have been used here to guide the choice of an indicative initial (highest) frame rate before undertaking the laboratory experiments on granular flow, they should be treated with some caution.

From their simplified simulation, [19] proposed a scheme to minimize the total error. The process should be analysed not only at the initial frame rate but also at different Δt obtained by skipping frames (i.e. increasing Δt) from the original recording. This strategy should continue until convergence to a single averaged value for a quantity (e.g. $\langle KE \rangle$) is reached. For gran-
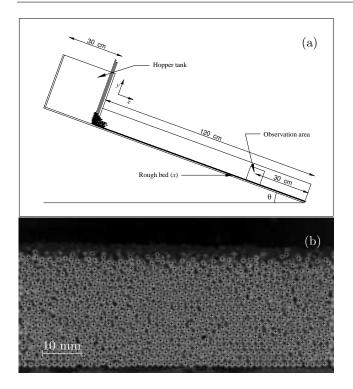
Fig. 4 Inclined chute geometry developed for the study of dry granular flows: (a) side view; (b) image detailed with positioned particle centres captured in the fully developed region of the flow.

ular flows, this is difficult to achieve, since as stated above, the flow characteristics (e.g. velocity gradient) vary with depth. A better choice would be to study the convergence of the KE profile rather than an averaged value. Analyses can be iterated by skipping frames until a value of Δt deemed close enough to those found in Fig. 3 is reached. This unique value will not be the correct one in all parts of the flow due to the change of velocity with depth, however, by employing values similar to those reported in Fig. 3 we can avoid using overly slow or fast frame rates, i.e., falling into areas where the error is severely dominated by particle position or acceleration uncertainties.

4.5 Outlier removal

Even with the best practice, PIV and PTV can return spurious vectors. However, there are a number of outlier detectors that can be used to remove these. One of the most commonly used is the median filter, also known as universal outlier detection. This method is based on defining a threshold value of the normalized residual velocity fluctuation of one data point relative to its neighbourhood. The data point is rejected when its residual is greater than the normalized residual thresh-

old. This approach is simple, computationally efficient and universal ([18]). Another filter worth mentioning is the mean local filter, which compares the direction and magnitude of each velocity vector with the local mean value of a pre-defined neighbourhood. This filter is very sensitive to the user-defined parameters required to consider a vector as outlier (size and number of points within the neighbourhood, maximum magnitude and angle difference between points), which can result in the elimination of a large number of correct vectors. [52] and [51] give more information on these two methods. In this paper these two filters were used during the processing of the data as reported in Sec. 5.2.

5 Experimental investigation on free-surface granular flows

5.1 Apparatus

The flume used in this study is a sloping rectangular 10 cm wide and 150 cm long channel that can tilt from horizontal up to 45° (Fig. 4(a)). At one end, the material is held inside a hopper, which can contain approximately 20 kg of material. A double-slider gate mechanism enables control of the releasing flow height that develops downstream. The basal roughness is created by gluing the flume bottom with the same material used to reproduce the granular flows. The walls are made of Perspex allowing observation at the sides. The sidewall surface of the granular flow of interest is illuminated by two 50W DC LED floodlights and captured via a high-speed camera (Phantom Miro 310).

The material used for the experiments was almost spherical ceramic beads (Sigmund Lindner Gmbh). This material was selected for several practical reasons: spherical particles are used in the majority of granular flow experiments, and accordant behaviour is assumed in many theories, while particle tracking algorithms often assume a spherical particle shape. The ceramic beads were nominally 1.4 - 1.6 mm in diameter with a bulk density of 2430 kg m^{-3}. The static friction angle, determined from a tilt test, was 24°.

5.2 Outline of the PIV and PTV procedures

The high-speed camera was positioned and aligned with the chute. Digital images of the moving mass were then recorded with a resolution of 256 x 256 pixels. The frame rate was varied: in this paper we report 1000 and 1400 fps as the maximum rate (Δt of 0.08 and approx. 0.06, respectively) depending on the velocity of

the flow. For each flow, a time series lasting 2 s - or $t = 162$ - (i.e. within the limit of our apparatus) was extracted from the original recording in the fully developed, steady region of the flow, about 30 cm before the outlet.

Following the scheme mentioned in Sec 4.2, we investigated the flows at the original frame rate and by progressively increasing the sampling interval by skipping one frame, i.e. doubling Δt, in each previous set. The additional frame rates obtained from the 1000 fps case were 500 fps, 250 fps and 125 fps (Δt equal to 0.16, 0.32 and 0.64). Similarly, for the 1400 fps case, 700 fps, 350 fps and 175 fps (Δt of approximately 0.12, 0.24 and 0.46), were produced. Note that increasing Δt to this extent brings its values within the interval highlighted in Fig. 3.

For the PIV analysis we employed the open source algorithm PIVLab ([49]). This particular PIV method uses a multi-pass approach to deform the interrogation areas in the second pass based on the estimate obtained in a previous one. For the multi-pass we selected 24 x 24 and 12 x 12 pixels, for the coarse and refined grid, respectively. Hence the analysis includes a state-of-the-art image deformation technique (e.g. [41]) which reduces the error associated with the correlation calculation by deforming the interrogation windows according to the local velocity gradient (shear deformation). We did not study the effect of smaller or larger areas on the results as in all cases the signal to noise ratio, defined as the ratio between the primary and secondary peaks in the correlation plane, was always reliable.

For PTV, the particle-tracking algorithm proposed by [13], briefly described earlier, was used. Upon the application of the centroid estimators, the outermost faint edges of the particles were removed by a morphological image opening. To do this we allowed the particles to have a diameter of approx. 5 pixel units. This conflicts somewhat with the diameter by which a particle should be approximated for a proper analysis in both PIV and PTV (3 pixels as shown in Fig 2). However, diameters smaller than 5 pixels would make the edges very difficult to recognize. Considering smaller particle diameters, i.e. 3 pixels, the particles could still be separated by a background subtraction. However, some particles would then result in being incorrectly approximated by single pixels and hence would be prone to pixel locking. For larger diameters, e.g. 5 pixels, the background subtraction affects the estimation of the centroid position only slightly. Following this procedure, the particle diameters in the image frames were reduced from the original 5 pixels down to approx. 3 pixels (e.g. see Fig. 1).

Although the particle images could be resized using background subtraction in this way, the particle-mask-correlation method alone still led to poor position estimates, due to the necessary thresholding used to remove the background. This was clearly revealed when the centroids were plotted over several frames. However, this information could be used to estimate particle locations for a least-squares method (e.g. as in Eq. 1), as discussed earlier.

The functional model for Eq. 1 was a Gaussian distribution, in this case a good approximation due to the spherical shape of the experimental material. The chosen parameter vector was $\boldsymbol{\theta} = (\tau_{00}, X_0, Y_0, d, \rho)$, where ρ is an additional factor in radian units, which allows for rotation of the pixel intensity grid associated with each particle, thus compensating for the surrounding particles. A sub-matrix was extracted from the original image around the guessed location. The characteristic brightness of a particle was isolated from the others (each giving the centroid coordinate with respect to one axis) and curves were fitted to the data (e.g. Fig. 1). This process was iterated for all the particles in the image. This scheme rendered the system considerably more stable over consecutive frames while improving the localization of the particle centroids at the same time.

The aforementioned processing steps were applied automatically to all successive images in the sequence. At a later stage, the tracking algorithm was initiated to sequentially match the particles in each pair of consecutive frames, producing arrays of particle displacement vectors. This arrangement was then filtered to remove erroneous and spurious displacements that contaminate the data by using the two filters mentioned in Sec 4.3.

Ultimately, both PIV and PTV require a transformation for relating information in pixels to physical lengths. Prior to each experiment, a calibration grid composed of regular circular marks spaced by 4 mm was located at the wall exactly in the region of interest. An image of this target grid was captured and the coordinates of the calibration marks detected with sub-pixel accuracy. These coordinates were then associated with an undistorted grid (mm units) and then interpolated by using the built-in Matlab function Scattered-Interpolant ([12]). The latter is an approach based on linear interpolation that uses Delaunay triangulation. The displacements are converted into real world coordinates and corrected for distortion induced by the imaging device and the optical distortions induced by the experimental facility.

5.3 Data processing

Upon completion of the PIV and PTV analyses, the resulting displacement data were used to compute the corresponding instantaneous and mean velocities. In PIV, the displacements obtained from cross-correlation divided by the sampling interval yields the components of the instantaneous velocity field (u_i, v_i), generally given in a regular mesh partitioned into rows and columns. The mean velocity is obtained as the temporal average of all velocities belonging to the same rows of interrogation regions (or columns depending on the flow direction) for the entire duration of the flow.

In PTV the in-plane instantaneous velocity is approximated by Eq. 2. Binning is then used to extract velocity profiles. The flow is subdivided into non-overlapping horizontal slices, typically of thickness one particle diameter. The mean velocities are then constructed by separately taking the ensemble-average velocities of each bin in the two directions.

As a general reference the slope-parallel (streamwise) mean velocity component $\bar{u}$ for each Kth bin/row is given by:

$$\bar{u} = \frac{\sum_{N_k}^{i=1} (u_i)_k}{N_k} \tag{3}$$

where N_k is the total number of velocity vectors in the Kth bin/row across the entire flow.

Another field property of interest in granular flows is the square of the velocity fluctuation, also known as the granular temperature. It provides a measure of the energy associated with the fluctuating nature of the granular motion, i.e. the agitation within the flow and is of importance to the transfer of stress via collisions. In this paper, we define granular temperature (T) from the measurement of fluctuation components. The slope-parallel fluctuation component is given as:

$$(u_i^*)_k = (u_i)_k - \bar{u}_k \tag{4}$$

The mean of the squares of this quantity is calculated for each bin/row as follows:

$$\langle (u^*)^2 \rangle_k = \frac{\sum_{N_k}^{i=1} [(u_i^*)^2]_k}{N_k} \tag{5}$$

Eqs. 3, 4 and 5 similarly apply to the slope-normal (transverse) velocity component v. The third component of velocity w was not measured in these experiments, thus the granular temperature is given as:

$$T_k = \frac{1}{2} \langle [(u_i^*)^2]_k + [(v_i^*)^2]_k \rangle \tag{6}$$

where the angle brackets denote ensemble averaging. By following this definition, granular temperature has units of squared velocity.

5.4 Estimation of density profiles

Measurements of solid concentration ν (or, alternatively, porosity $\phi = 1 - \nu$), defined as the ratio of volume occupied by the solid to the total volume, are useful to examine the dependency of basic flow properties such as velocity and granular temperature on ν. To date, simple, cost effective and very accurate measurements of this quantity are still challenging to reproduce, especially for dense and opaque systems. In the following we describe simple methods used to estimate two- and three-dimensional solid concentration profiles based on image analysis and information obtained from the centroiding procedure for PTV.

In our particular case, the fact that the flows are made of spherical, nearly uniform, particles can be exploited to obtain concentration profiles. If the particles can be visualized at a sufficient pixel scale, their edges can be easily distinguished and an algorithm can be used such as that based on the Hough transform for finding circles in a image ([9]). While keeping the same chute conditions (i.e. inclination and gate height), we performed similar flows to those we used to measure other properties derived from the velocity fields but at a larger spatial resolution. In these experiments the particles were approximated to ≈ 27 pixels in diameter compared to the 5 pixels adopted to minimize the particle position errors. This was necessary to improve the robustness of the Hough transform detection and remove spurious circular shapes developed at smaller scales. Prior to the direct application of the Hough transform, a morphological image opening was applied to the image to enhance the foreground particles. The particle circumferences of the first layer closest to the side-wall were then outlined by the edge detector. Images were subdivided into bins (27 pixels in height), which in turn allowed for the calculation of the particle areas (the entire area or part if the particle was shared across two bins). The sum of all areas divided by the total area of the corresponding bin yielded the value of two-dimensional solid concentration.

It should be noted that the results are affected by the side-walls and may not represent accurately the local solid concentration throughout. The algorithm also is not able to isolate particles leaving the side-walls unless the particle partially disappears behind the first layer. We assumed that the particles remained close to the side-walls for a long enough period of time, although this may not be the case, especially at steeper

slopes. Furthermore, the algorithm has the tendency to construct smaller circumferences than the real particle edges leading to underestimations in the data with an estimated error of up to 4%. To examine this we varied specific parameters (e.g. the minimum and maximum radii required for the detection of circles) which resulted in slightly differences in magnitude of solid concentration while the profiles changed little.

In the three-dimensional case, concentrations may be theoretically estimated from the point density of visible particles per unit image surface ([1]). However, this method is limited to sparse dispersions and becomes unsuitable for dense flows due to the prevalence of occlusion effects ([15]). On the other hand, when the mean interparticle distance becomes of the order of the diameter (as in the case of dense systems) neighbouring particles are forced to organize with respect to each other into increasingly ordered assemblies. This creates short-range correlations between grain positions allowing the characterization of the local particle arrangement with local descriptors, as proposed by [15]. The ordering can be estimated based on the roundness of the Voronöi polygons. From the centroiding procedure for PTV (see Sec. 4.2), these can be constructed based on the known position of each particle and those of the surrounding ones. Depending on the local concentration of the system each particle has its own configuration (a polygon with a certain number of sides). The shape of the polygon can then be related to the concentration via a Voronöi-base indicator. This is provided by the ratio $\xi = 4\pi A/P^2$, where A and P are the area and perimeter of the polygon, respectively. Once the flow has been divided into horizontal slices (or bins as described in Sec. 4.3) a local average value of ξ is obtained for a sufficient number of individual polygons over time. This average value ($\bar{\xi}$) is then used to determine a three-dimensional granular concentration profile based on the normalized power law relation calibrated by [15]:

$$\frac{\nu}{\nu_{rcp}^{3D}} = \left(\frac{\bar{\xi} - \xi_{min}}{\xi_{rcp} - \xi_{min}}\right)^{\beta} \tag{7}$$

where ν is the solid concentration of the solid material, $\nu_{rcp}^{3D} \approx 0.64$, i.e. the 3D random close packing for spheres and $\xi_{min} \approx 0.72$, which derives from Monte-Carlo simulations ([35]). The other parameters, $\xi_{(rcp)} = 0.84$ and $\beta = 3.5$ were calibrated by [15] based on fluidization cell tests.

The validity of this method has also been tested by [30] based on a comparison with 3D stereoscopic measurements. He found that correct values of solid concentration based on roundness estimate of the Voronöi polygons can be extended up to $\nu \approx 0.55$. Hence, it is

not expected that Eq. 7 applies for very densely packed systems. Other effects (e.g. particle shape or sidewalls) in addition to volume exclusion can contribute to the ordering of the particles leading to an erroneous solid concentration estimation. When the pattern-based estimator is used, such effects can lead to unreasonably high concentration values. Therefore, a limiting maximum concentration (ν_{rcp}^{3D}) must be imposed ([6]). In other words, all the values that exceed this threshold are assumed to be in the maximum packing state ν_{rcp}^{3D}. It is also expected that in the range $0.55 < \nu < \nu_{rcp}^{3D}$ the results yield only an approximate indication of ν.

A great deal of research has been devoted to the improvement of solid concentration measurements. For near-wall granular flows, a three-dimensional imaging technique with a multiple-camera system can be used to obtain such measurements. [44] showed how this method is able to overcome occlusion effects and is suited for highly concentrated and rapidly moving dispersions. Alternatively, [45] proposed a methodology to measure concentrations based on the image analysis of near-wall grains (either in dry or fluid saturated condition) by means of a laser-illuminated sheet shone laterally to the flows and recorded by a single camera. This laser-based technique was found to yield good estimates of concentration. Both methodologies represent valuable alternatives, however, for the purpose of this work we sought only to adopt approaches that are easy to implement with simple systems (e.g. monocular imaging with simple lighting) and reduced costs.

Applications of the two methods previously described (namely, high resolution images and pattern-based indicator) are reported and compared in Fig. 6 (e,f). While the maximum theoretical value of ν for spheres varies in the two cases ($\nu_{rcp}^{2D} \approx 0.82$ and $\nu_{rcp}^{3D} \approx 0.64$, respectively), the profiles show a similar variation of the concentration with depth. Some discrepancies arise in the first layer of the two-dimensional profiles at 26°. This point represents firmly glued particles at the bottom and should not be taken into consideration. Notably, both approaches have their strengths and limitations. High resolution images tend to underestimate the concentration. Conversely, the roundness indicator leads to an overestimation in most cases which is corrected by limiting the maximum value that can be achieved. However, these methods can still be used to assess the variation of other kinematic properties of the flows, as described in Sec. 6.1.

6 Results

For the purpose of this work, we wish to bring attention to two granular flows released at an inclination of 26°

and 30°, respectively. In both cases the experimental conditions (mass and flow rate) were kept constant, producing nominal, steady, flow depths of approximately 18 particle diameters over a sampling period of $t = 162$. Over the duration considered, the slope-normal component of velocity (v) showed in all cases a gradient very close to zero with a tendency to deviate from it at the free surface due to the higher mobility of the flows. Thus, to take this effect into account, in the calculations of granular temperature the two velocity components (u, v) in Eq. 6 are summed together and only one curve is plotted for each experiment at different Δt.

Distributions of the mean (ensemble-averaged) velocities obtained from the PIV algorithm are given in Fig. 5 (a,b). For each flow, the velocity profiles collapse onto a single curve for different Δt, indicating a lack of sensitivity to time step over the range considered. The magnitude of the streamwise mean velocity increases with steeper inclination as expected and a higher velocity is found at the free-surface, decreasing with depth until the bed of the chute is encountered. The first layer of particles appearing at the bottom through the sidewall is firmly glued, so that no-slip velocity is exhibited. Thus, zero basal slip velocity is always found.

Profiles of granular temperature using PIV, as defined in Eq. 6 are given in Fig. 5 (c,d). This ensemble-average quantity achieves its maximum value at the free surface and decays to zero with depth. When plotted on the same graph, the granular temperature distributions in each flow have similar values but when the flows are processed with the two largest Δt (≈ 0.24 and ≈ 0.46) some dissimilarities in the profile of granular temperature arise. They are caused by faster moving particles that leave the sub-image causing loss of correlation. Most importantly, the magnitude of granular temperature profiles is rather less than that measured by PTV (Fig. 6 (c,d)) as explained later in more detail. The reason for this may be due to the size of the interrogation region. In these experiments we chose 12 x 12 pixels as the smallest interrogation window which can contain a maximum of approx. 5 particles (the least seeding concentration required for a correct correlation peak localization). This implies that the measured values are not referred to a single particle but to an ensemble. In other words, averaging and smoothing of the data is introduced, which may damp the fluctuations measured. One could perform an analysis with very small interrogation areas to mitigate this, although this would make the correlation peak very difficult to identify resulting in potentially inaccurate displacement estimates. This approach was previously trialled for sub-images having size of the order of one particle diameter ([20]) - although this used a different PIV algorithm and particle image diameter - with results suggesting that PIV may, in general, produce lower estimates of granular temperature than PTV.

An alternative approach was presented by [39]. From a coarse PIV analysis, i.e. using interrogation regions larger than the particle diameter, they showed that the values of granular temperature can be theoretically scaled to the characteristic length scale of one particle diameter. When scaled, the results are useful to directly compare with the PTV results which are obtained from the tracking of single particles. Following their approach we scaled up our measurements by a factor of 9 with values reported in Fig. 5 (e,f). The scale factor can be calculated considering the actual interrogation size (δ_{act}), in our case 12 pixels, and as the interrogation area is decreased by a factor n the calculated granular temperature will increase by the same factor leading to $n = (\delta_{act}/\delta_p)^2$, where δ_p is the presumed interrogation area including one image particle. With $\delta_p = 4$ (somewhat larger than 3 pixels to take into account any change in particle shape and dimension) the scale factor by which the measurement are increased is $(12/4)^2 = 9$.

Mean velocity profiles produced by PTV are shown in Fig. 6 (a,b). As with PIV, velocity profiles collapse onto a single curve for different sampling intervals, although the velocity measured at $\Delta t \approx 0.46$ becomes corrupted above a depth of 12 particles. At this frame rate the PTV algorithm is incapable of correctly performing the matching routine due to the large displacements and a few velocity vectors from which to calculate the average. Without considering this particular case, the magnitude of the velocities is very similar to those found for PIV (Fig. 5 (a,b)), which cross-validates the particle tracking and particle image velocimetry algorithms, at least in terms of mean velocity.

Distributions of granular temperature obtained with PTV are shown in Fig. 6 (c,d), where the most notable feature is the variability of granular temperature with Δt (or frame rate). That is, although the mean velocity measurement is insensitive to Δt, the determined granular temperature is greatly influenced by it. As is clear in Fig. 6 (c,d), there is a shift of the granular temperature profiles to the left with increase in Δt, converging somewhat at large Δt although the exact values do not (they are still declining with Δt). However, this trend disappears for sampling intervals smaller than 0.16 and approx. 0.12, respectively. The reason for this is that errors in the determination of the square of the fluctuation velocities accumulate (rather than cancel out) during the ensemble-average calculations. Conversely, for the mean velocities, the errors in instantaneous velocities are reduced by averaging.
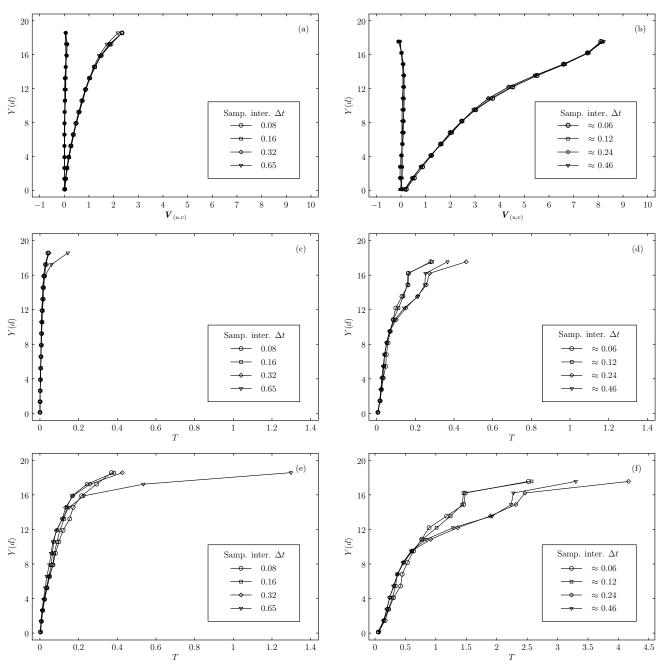
Fig. 5 Depth-averaged flow property profiles obtained with PIV at different sampling intervals (Δt): (a,b) mean velocity for the flows released at an inclination of 26° and 30°. Filled symbols represent transverse (v) velocity, empty symbols streamwise (u) velocity; (c,d) granular temperature at 26° and 30°; (e,f) granular temperature scaled up by a factor of 9.

When PTV data is compared to PIV results, the shape of the granular temperature profiles show similar trends, i.e., increasing values moving towards the free-surface and an apparent change in the gradient above 10 particle diameters in the flow at 30°. For the same flow at 26° the magnitude is slightly higher while at an inclination of 30° the dimensionless granular temperature reaches values up to 4.2 at the flow surface which are well beyond the average magnitude showed in the

rest of the analyses. This is probably caused by the errors arising during the cross-correlation process in PIV which are then magnified when granular temperature is scaled up.

Looking at the data for both PIV and PTV we recognize the expected changes of granular temperature. High-speed images at the base near the side-wall indicates frictional dependence of the motion with occasional brief contacts between neighbouring particles

and more long-lived contacts (i.e. less granular temperature is generated). In contrast, particle collisions become more prominent towards the free-surface (i.e. more granular temperature is produced). Additionally, the granular temperature increases with increasing tilt angles, as the kinetic energy of the system increases.

6.1 Granular temperature sensitivity on density profiles

In simple dry granular shear flows down inclined geometries, three different regimes can be usually identified: a quasi-static regime governed primarily by inter-particle friction, a dense flow regime where grains interact both through enduring contacts and through collisions, and as the granular material gradually accelerates it becomes more agitated until it reaches a collisional-dominated rapid flow regime. These three regimes can coexist and are strictly connected to the shear rate γ (the rate of change of velocity across the shear flow) and the solid fraction profile.

Granular temperature is a by-product of particle collisions, and has been shown to follow the same order of magnitude as the shear rate γ ([32]). This relation is depicted in Fig 6 (g,h) for the flows studied here. For clarity, we have omitted the data related to the shortest sampling intervals which appear to be dominated by the accumulation of errors. When the particle concentration decreases with the shear rate, i.e., when the system becomes diluted, individual particles experience random collisions which are converted through grain velocity into higher flow mobility. This can be expected to happen close to the free surface of simple dry granular flows where the stress associated with the granular temperature acts to force the particles apart thus creating a dilute region represented by lower solid fraction.
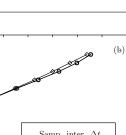
After these considerations, we compare the values of granular temperature calculated here with the solid fraction profiles in two and three-dimensions. Note that the profile for $\Delta t \approx 0.06$ in Fig 6 (d) is affected by the high accumulation of errors and should not be considered below. The gradient of granular temperature developed in the body of the flow at an angle of 26° steadily increases, remaining close to zero until some more agitation (or granular temperature) is produced at the free surface. In contrast, the flow released at 30° shows a clear change of granular temperature above 10-12 particle diameters (depending on the solid concentration considered) which is accompanied by a growing dilated region. These features are captured by the solid concentration profiles shown in Fig. 6 (f). For 26° we see that the solid concentration is nearly uniform in the central part of the flow but changes when the free-surface is
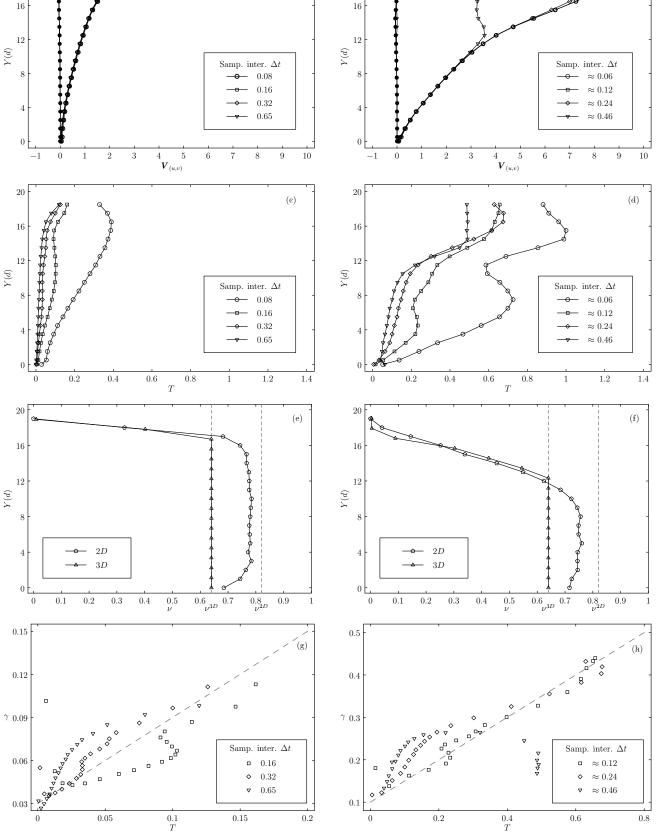
approached. For 30° the solid concentration decreases significantly above 10-12 particle diameters showing the flow to be more diluted. The good agreement between the changes of granular temperature and the profiles of solid fraction confirms the general variations expected in these flows and supports the validity of our measurements.

7 Conclusions

Particle image velocimetry (PIV) and particle tracking velocimetry (PTV) were briefly reviewed and the common sources of error and the methods used for their reduction were discussed. It was found that the errors originating from PIV procedures can be mitigated by an appropriate selection of the interrogation region size and the particle image diameter. To our knowledge, error frameworks associated with PTV only exist for steady and long-lasting granular flows (e.g in a recirculating flume ([6,31])). The difficulties with quasi-steady and short-lasting flow measurements (as in dam-break experiments) is that, by definition, steady flows are not obtained. Hence, this work has focused on the removal of potential sources of error affecting measurements of granular temperature that could be *a priori* avoided, rather than methods to deal with these in a *post hoc* situation. For this technique, two main errors were described and analysed, those associated with the particle centroid estimates and with the particle acceleration. We found that the former is reduced for particle image diameters of approximately 3 pixel (for monodisperse granular flows). The latter requires an appropriate choice of the sampling interval (or frame rate). Indeed, there should be a frequency of acquisition where the aforementioned errors are minimized. We used a simple simulation of a circular motion which may help in choosing a most appropriate sampling interval. Notably, high frame rate can greatly worsen velocity errors and compromise the results.

We studied the influence of these observations on different granular flows down an inclined geometry. The results of mean velocity were well matched by the two techniques, which allowed the two algorithms to be cross-validated, at least in terms of this quantity. Conversely, rather different profiles of granular temperature where obtained between the two methods. Granular temperature profiles for PIV were somewhat sampling-interval dependent with magnitudes that increased at larger Δt, specifically at $\Delta t = 0.65$ for a slope of 26° and more clearly at $\Delta t \approx 0.24$ and 0.46 for a slope of 30°. This effect was associated with the selection of the sample interval which caused loss of correlation at large Δt. Moreover, errors in the PIV results are also likely to

Fig. 6 Depth-averaged flow property profiles obtained with PTV at different sampling intervals (Δt): (a,b) mean velocity for the flows released at an inclination of $26°$ and $30°$. Filled symbols represent transverse (v) velocity, empty symbols streamwise (u) velocity; (c,d) granular temperature at $26°$ and $30°$; (e,f) 2D and 3D solid concentrations. Dashed lines represent the two theoretical limits ν_{rcp}^{2D} and ν_{rcp}^{3D}; (g,h) ratio of shear rate to granular temperature.

be connected with the scale of scrutiny used in the analysis. Therefore, careful judgement has to be made not only when choosing the sampling interval, but also when deciding the spatial resolution of interest. We selected an interrogation size that included several particles in order to minimize the error associated with the correlation peak localization. Considerably different values for the directly measured and theoretically scaled second-order-statistical quantities (i.e. granular temperature) were obtained when compared to PTV results. The direct application of Eq. 6 showed a notable underestimation of these values. The opposite was obtained after scaling according to the method proposed by [39], with values that were magnified and much larger than expected, especially for the 30° case. Conducting such a scaling analysis on the PIV results to enable granular temperature to be derived from measurements over large interrogation regions did not generate the expected results, and it still remains unclear whether PIV can be used for this purpose.

The same sampling interval dependency but with an opposite trend was seen in the PTV results, with both changes in granular temperature magnitude and profile shape. The accumulation of errors for the smallest Δt (≈ 0.06 and 0.08) produced very different profiles when compared to the rest. Nonetheless, for the largest Δt (≈ 0.46 and 0.65) PTV was only partially able to obtain correct measurements away from the surface of the flows, as it is evident above 12 particle diameters for $\Delta t \approx 0.46$ in Fig 6(d). If these values are disregarded, the remaining agree qualitatively with those of PIV, i.e., although the shape of the profiles are similar the values are not. For this data the general variation of granular temperature were also supported by our estimations of the solid concentration.

Granular temperature results obtained from the PIV and PTV analyses were unexpectedly variable and both methods had shortcomings when applied to dense granular flows. A more detailed analysis is underway where results from discrete element simulation of dry granular flows are used to generate synthetic images with known particle locations. The two imaging techniques will be tested against these images in order to compare their results against the true velocity and granular temperature determined numerically, and thus we should be able to infer which one is the more appropriate technique to be used for these types of analyses.

References

1. Adrian, R.J, Particle-imaging techniques for experimental fluid mechanics, Annual Review of Fluid Mechanics, 23(1), 261-304 (1991)
2. Adrian, R.J., Dynamic ranges of velocity and spatial resolution of particle image velocimetry, Measurement Science and Technology, 8(12), 1393 (1997)
3. Adrian, R.J., Twenty years of particle image velocimetry, Experiments in Fluids, 39(2), 159-169 (2005)
4. Adrian, R.J., Westerweel, J., Particle image velocimetry, Cambridge University Press, Cambridge (2011)
5. Ancey, C., Andreini, N., Epely-Chauvin, G., Granular suspension avalanches. I. Macro-viscous behaviour, Physics of Fluids, 25(3), 033301 (2013)
6. Armanini, A., Capart, H., Fraccarollo, L., Larcher, M., Rheological stratification in experimental free-surface flows of granularliquid mixtures, Journal of Fluid Mechanics, 532, 269-319 (2005)
7. Azanza, E., Chevoir, F., Moucheront, P., Experimental study of collisional granular flows down an inclined plane, Journal of Fluid Mechanics, 400, 199-227 (1999)
8. Bagnold, R.A., Experiments on a gravity-free dispersion of large solid spheres in a Newtonian fluid under shear, Proceedings of the Royal Society of London. Series A. Mathematical and Physical Sciences, 225(1160), 49-63 (1954)
9. Ballard, D.H., Brown, C.M., Computer vision, Prentice Hall Inc, Englewood Cliffs, N.J, (1982).
10. Berryman, J.G., Random close packing of hard spheres and disks, Physical Review A, 27(2), 1053-1061 (1983)
11. Bi, W., Delannay, R., Richard, P., Valance, A, Experimental study of two-dimensional, monodisperse, frictional-collisional granular flows down an inclined chute, Physics of Fluids, 18(12), 123302 (2006)
12. Brevis, W., García-Villalba, M., Shallow-flow visualization analysis by proper orthogonal decomposition, Journal of Hydraulic Research, 49(5), 586-594 (2011)
13. Brevis, W., Niño, Y., Jirka, G.H., Integrating cross-correlation and relaxation algorithms for particle tracking velocimetry, Experiments in Fluids, 50(3), 135-147 (2011)
14. Bryant, S.K., Take, W.A., Bowman, E.T., Observations of grain-scale interactions and simulation of dry granular flows in a large-scale flume, Canadian Geotechnical Journal, 52(5), 638-655 (2015)
15. Capart, H. & Young, D.L. & Zech, Y., Voronoï imaging methods for the measurement of granular flows, Experiments in Fluids 32(1), 121-135 (2002)
16. Cierpka, C., Lütke, B., Kähler, C.J., Higher order multi-frame particle tracking velocimetry, Experiments in Fluids, 54(5), 1533 (2013)
17. Cowen, E.A., Monismith, S.G., A hybrid digital particle tracking velocimetry technique, Experiments in Fluids, 22(3), 199-211 (1997)
18. Duncan, J., Dabiri, D., Hove, J., Gharib, M., Universal outlier detection for particle image velocimetry (PIV) and particle tracking velocimetry (PTV) data, Measurement Science and Technology, 21(5), 057002 (2010)

19. Feng, Y., Goree, J., Liu, B., Errors in particle tracking velocimetry with high-speed cameras, Review of Scientific Instruments, 82(5), 053707 (2011)

20. Gollin, D., Bowman, E.T., Shepley, P, Methods for the physical measurement of collisional particle flows, IOP Conference Series: Earth and Environmental Science, 26(1), 012017 (2015)

21. Hain, R., Kähler, C.J., Fundamentals of multi-frame particle image velocimetry (PIV), Experiments in Fluids, 42(4), 575-587 (2007)

22. Hanes,D.M., Walton, O.R., Simulations and physical measurements of glass spheres flowing down a bumpy incline, Powder Technology, 109(1-3), 133-144 (2000)

23. Hart, D.P., PIV error correction, Experiments in Fluids, 29(1), 13-22 (2000)

24. Hassan, Y.A., Blanchat, T.K., Seeley, C.H., PIV flow visualization using particle tracking techniques, Measurement Science and Technology, 3(7), 633642 (2000)

25. Holyoake, A.J., McElwaine, J.N., High-speed granular chute flows, Journal of Fluid Mechanics, 710, 35-71 (2012)

26. Jain, N., Ottino, J.M., Lueptow, R.M., An experimental study of the flowing granular layer in a rotating tumbler, Physics of Fluids, 14(2), 572-582 (2002)

27. Jenkins, J.T., Dense inclined flows of inelastic spheres, Granular Matter, 10(1), 47-52 (2007)

28. Jop, P., Forterre, Y., Pouliquen, O., Crucial role of sidewalls in granular surface flows: consequences for the rheology, Journal of Fluid Mechanics, 541, 167- 192 (2005)

29. Keane, R.D. and Adrian, R.J., Theory of cross-correlation analysis of PIV images, Applied Scientific Research, 49(3), 191-215 (1992)

30. Larcher, M., Vertical Structure of High Concentration Liquid-Granular Flows, Monographs of the School of Doctoral Studies in Environmental Engineering, University of Trento, Vol. 2, 151 p. (2004)

31. Larcher, M., Fraccarollo, L., Armanini, A., Capart, H., Set of measurement data from flume experiments on steady uniform debris flows, Journal of Hydraulic Research, 45(sup1), 5971 (2007)

32. Losert, W. & Bocquet, L. & Lubensky, T. C. & Gollub, J.P., Particle Dynamics in Sheared Granular Matter , Physical Review Letters 85(7), 14281431. (2000)

33. Maas, H.G., Gruen, A., Papantoniou, D., Particle tracking velocimetry in three-dimensional flows, Experiments in Fluids, 15(2), 133-146 (1993)

34. Ohmi, K., Li, H., Particle-tracking velocimetry with new algorithms, Measurement Science and Technology, 11(6), 603 (2000)

35. Okabe, A. & Boots, B. & Sugihara, K., Spatial tessellation: Concepts and applications of Voronoï diagrams, Wiley, New York (1992)

36. Owaga, S., Multi-temperature theory of granular materials, In Proceedings of US-Japan Seminar on Continuum-Mechanical and Statistical Approaches in the Mechanics of Granular Materials, Tokyo, 208-217 (1978)

37. Prasad, A.K., Adrian, R.J., Landreth, C.C., Offutt, P.W., Effect of resolution on the speed and accuracy of particle image velocimetry interrogation, Experiments in Fluids, 13(2-3), 105-116 (1992)

38. Pudasaini, S.P., Hutter, K., Hsiau, S., Tai, S., Wang, Y., Katzenbach, R. Rapid flow of dry granular materials down inclined chutes impinging on rigid walls, Physics of Fluids, 19(5), 053302 (2007)

39. Reynolds, G.K., Nilpawar, A.M., Salman, A.D., Hounslow, M.J., Direct measurement of surface granular temperature in a high shear granulator, Powder Technology, 182(2), 211-217 (2008)

40. Scarano, F., Riethmuller, M. L, Advances in iterative multigrid PIV image processing, Experiments in Fluids, 29(1), S051-S060 (2000)

41. Scarano, F., Iterative image deformation methods in PIV, Measurement Science and Technology, 13(1), R1 (2002)

42. Scarano, F., Tomographic PIV: principles and practice, Measurement Science and Technology, 24(1), 012001 (2013)

43. Schaefer, M., Bugnion, L., Kern, M., Bartelt, P., Rapid flow of dry granular materials down inclined chutes impinging on rigid walls, Granular Matter, 13(2) 327-336 (2010)

44. Spinewine, B. & Capart, H. & Larcher, M. & Zech, Y., Three-dimensional Voronoï imaging methods for the measurement of near-wall particulate flows, Experiments in Fluids 34(2), 227-241 (2003)

45. Spinewine, B. & Capart, H. & Fraccarollo, L. & Larcher, M., Laser stripe measurements of near-wall solid fraction in channel flows of liquid-granular mixtures, Experiments in Fluids 50(6), 1507-1525 (2011)

46. Stanier, S.A., Blaber, J., Take, W.A., White, D., Improved image-based deformation measurement for geotechnical applications, Canadian Canadian Geotechnical Journal 53(5), 727-739, (2015)

47. Takehara, K., Etho, T., A study on Particle Identification in PTV - Particle Mask Correlation Method, Journal of Visualization, 1(3), 313-323 (1999)

48. Tischer, M., Bursik, M.I., Pitman, E.B., Kinematics of Sand Avalanches Using Particle-Image Velocimetry, Journal of Sedimentary Research, 71(3), 355-364 (2001)

49. Thielicke, W., Stamhuis, E.J., PIVlab - Towards User-friendly, Affordable and Accurate Digital Particle Image Velocimetry in MATLAB, Journal of Open Research Software, 2(1), 355-364 (2014)

50. Warr, S., Jacques, G.T.H., Huntley, J.M., Tracking the translational and rotational motion of granular particles: Use of high-speed photography and image processing, Powder Technology, 81(1), 41-56 (1994)

51. Westerweel, J., Efficient detection of spurious vectors in particle image velocimetry data, Experiments in Fluids, 16(3-4), 236-247 (1994)

52. Westerweel, J., Scarano, F., Universal outlier detection for PIV data, Experiments in Fluids, 39(6), 1096-1100 (2005)

53. White, D.J., Take, W.A., Bolton, M.D., Soil deformation measurement using particle image velocimetry (PIV) and photogrammetry, Géotechnique, 53(7), 619-631 (2003)